



Feasibility of intravoxel incoherent motion in the assessment of tumor microvasculature and blood–brain barrier integrity: a case-based evaluation of gliomas

Andre Monteiro Paschoal^{1,2,3} · Maria Clara Zanon Zotin^{2,4} · Lucas Murilo da Costa³ · Antonio Carlos dos Santos² · Renata Ferranti Leoni³

Received: 30 June 2021 / Revised: 5 December 2021 / Accepted: 6 December 2021 / Published online: 15 December 2021
© The Author(s), under exclusive licence to European Society for Magnetic Resonance in Medicine and Biology (ESMRMB) 2021

Abstract

Objective To evaluate the feasibility of intravoxel incoherent motion (IVIM) in assessing blood–brain barrier (BBB) integrity and microvasculature in tumoral tissue of glioma patients.

Methods Images from 8 high-grade and 4 low-grade glioma patients were acquired on a 3 T MRI scanner. Acquisition protocol included pre- and post-contrast T1- and T2-weighted imaging, FLAIR, dynamic susceptibility contrast (DSC), and susceptibility-weighted imaging (SWI). In addition, IVIM was acquired with 15 b-values and fitted under the non-negative least square (NNLS) model to output the diffusion (D) and pseudo-diffusion (D*) coefficients, perfusion fraction (f), and f times D* (fD*) maps.

Results IVIM perfusion-related maps were sensitive to (1) blood flow and perfusion alterations within the microvasculature of brain tumors, in agreement with intra-tumoral susceptibility signal (ITSS); (2) enhancing areas of BBB breakdown in agreement with DSC maps as well as areas of BBB abnormality that was not detected on DSC maps; (3) enhancing perfusion changes within edemas; (4) detecting early foci of increased perfusion within low-grade gliomas.

Conclusion The results suggest IVIM may be a promising approach to delineate tumor extension and progression in size, and to predict histological grade, which are clinically relevant information that characterize tumors and guide therapeutic decisions in patients with glioma.

Keywords Intravoxel incoherent motion · Gliomas · Microvasculature · Blood–brain barrier

Introduction

Gliomas are a critical and heterogeneous class of primary brain tumors originating from the glial cells, representing about 50% of all cerebral neoplasm [1]. The WHO

classification system subdivides gliomas according to histopathological grade and molecular profile [1]. For example, it is well known that glioblastomas (GBMs, grade 4) and isocitrate dehydrogenase (IDH) wild type tumors are typically aggressive, with poor prognosis. In contrast, low-grade gliomas (LGG, grades 1 and 2) encompass a more heterogeneous group of tumors with variable clinical prognosis [1].

Histopathological analysis with molecular phenotyping is the gold-standard approach for tumor classification, but the quest for noninvasive alternatives capable of offering relevant diagnostic and prognostic information remains. In that sense, several magnetic resonance imaging (MRI) techniques have been increasingly used to enhance brain tumors characterization and predict histopathological grade and biological behavior. Among the many promising MRI techniques in neuro-oncology, contrast-free perfusion imaging has gained increased attention. Performed alongside contrast-enhanced sequences, it allows for better characterization of

✉ Andre Monteiro Paschoal
andre.paschoal@hc.fm.usp.br

¹ LIM44, Instituto e Departamento de Radiologia, Faculdade de Medicina, Universidade de São Paulo, São Paulo, SP 05403-010, Brazil

² Medical School of Ribeirao Preto, University of Sao Paulo, Ribeirao Preto, SP 14040-900, Brazil

³ InBrain Lab, FFCLRP, University of Sao Paulo, Ribeirao Preto, SP 14040-900, Brazil

⁴ Department of Neurology, Massachusetts General Hospital, Harvard Medical School, Boston, MA, USA

tumor hemodynamics, which directly reflects tumor aggressiveness [2–4]. Specifically, contrast-free perfusion imaging evaluates tumor microvasculature and offers several advantages over gadolinium-based techniques. It does not require a precise knowledge of the injection parameters and does not expose the patient to eventual gadolinium collateral effects, or to potential tissue retention effects. Susceptibility-weighted imaging (SWI) is also useful to analyze glioma's microvasculature. Intratumoral susceptibility signal (ITSS) has been related to intralesional hemorrhage, calcification, and neovascularity, contributing to glioma histopathological characterization [5, 6].

Among the contrast-free perfusion imaging approaches alternatives, intravoxel incoherent motion (IVIM) is an MRI method that explores a scaling in diffusion weighting to infer diffusion and perfusion information simultaneously by separating each contribution of the total signal measured [4, 7]. In contrast, arterial spin labeling (ASL) uses the arterial blood as an endogenous tracer magnetically labeled through the application of radiofrequency (RF) pulses [8, 9]. Although ASL is well established in the literature with a broad range of clinical applications [10], it suffers from limitations related to signal intensity decays with the longitudinal relaxation time (T_1), hampering the analysis for patients with very long arterial transit time, which is the case for the perfusion in white matter. On the other hand, since IVIM explores the diffusion movement of water molecules, it is not dependent on the arterial transit time. Also, like ASL [11], IVIM allows for the characterization of microvascular perfusion within the tumor. Previous studies have already reported the success of IVIM in glioma grading [12–18].

Though the categorization of gliomas in different grades contributes to harmonizing diagnosis and therapeutic approaches, the genetic, metabolic, and morphological abnormalities that underlie tumor progression occur instead as a continuum and help explain how tumors of similar grades may present heterogeneous evolution patterns. Identifying early signs of tumor progression through neuroimaging biomarkers can guide appropriate and prompt therapeutics and has become a research priority. It is especially important for LGG, in which MRI markers can predict evolution to HGG, demanding a more aggressive treatment. It is well known that high-grade gliomas (HGG, grades 3 and 4) develop an extensive microvascular tree, with BBB disruption [19]. Accordingly, MRI techniques able to capture such perfusion and permeability abnormalities may serve as biomarkers, predicting prognosis and evolution of gliomas.

In this case series, we aimed to evaluate how IVIM findings in HGG can be associated with increased microvascular perfusion and BBB damage by comparing such findings against more established markers (perfusion maps extracted from dynamic susceptibility contrast (DSC), microvascular signal of ITSS obtained from SWI, and hyperintensities in

post-contrast FLAIR) and assessing whether they offer complementary information. Furthermore, we assessed whether IVIM findings in LGG could capture microvasculature changes predictive of earlier evolution to HGG.

Methods

Subjects

Twelve patients (8 HGG, 4 LGG; mean age \pm standard deviation (SD) = 56.11 ± 19.14) participated in this cross-sectional study, approved by the Institutional Review Board, after signing the informed consent agreement. Patients were recruited at the Clinical Hospital of the Institution, and the inclusion criteria were presence of glioma compatible findings in the MR images, confirmed and characterized through histopathological analysis. Exclusion criteria were previous surgical intervention, non-glioma final diagnosis (e.g., germline neoplasms, colorectal metastasis, infectious lesions), pregnancy, claustrophobia, and contraindications for MRI. The sample size was determined by the number of patients who met the criteria and agreed to participate in the study.

MR system

Data were acquired at a 3 T MR system (Achieva, Philips Medical System, The Netherlands), equipped with gradients of 80 mT/m amplitude and 200 mT/m/ms slew rate. A vendor standard transmit body coil, and a 32-channel receive-only head coil were used to measure the signal.

Scanning protocols

Patients were scanned under the Institution clinical protocol for tumors, which consists of whole-brain three-dimensional T1-weighted images (3D-T1W GRE) acquired pre- and post-gadolinium injection, three-dimensional fluid-attenuated inversion recovery (FLAIR), axial T2-weighted images, MR spectroscopy (MRS), dynamic susceptibility contrast (DSC) T2*-weighted perfusion images, high-resolution diffusion-weighted images (DWI) and high-resolution susceptibility-weighted images (SWI), and the addition of IVIM images using 15 b-values (0, 4, 8, 16, 30, 60, 120, 250, 500, 1000, 1200, 1400, 1600, 1800 and 2000s/mm²). Table 1 shows the description of the complete parameters of the whole protocol.

Data processing

IVIM and DSC data preprocessing were performed in SPM12 (Wellcome Trust Center for Neuroimaging, University College London, UK). For IVIM data, the preprocessing

Table 1 Data acquisition parameters

	3D T1W	AXIAL T2W	3D FLAIR	MRS	DSC	HR DWI	HR SWI	IVIM
FOV (mm ²)	240×240	240×240	240×240	200×180	240×240	240×240	240×240	240×240
Spatial resolution (mm ²)	1×1	0.39×0.39	0.6×0.6	0.45×0.63	1.44×1.44	2×2	0.43×0.43	2×2
Slice thickness (mm)	1	3	1	1.1	5	4	4	5
Number of slices	180	50	180	96	24	150	150	20
TR (ms)	7	6620	5000	20	17	2900	15.8	3000
TE (ms)	3.2	80	334.21	3.45	25	68	22.4	102
TI (ms)	–	–	1600	–	–	–	–	–
FA (degrees)	8	90	90	20	90	90	15	90
Number of repetitions	1	1	1	1	70	1	1	1
Number of b-values	–	–	–	–	–	2	–	15
Total scan time (min)	5.98	3.09	3.83	3.58	1.86	1.17	2.17	4.20

included motion correction, while correction for eddy current and susceptibility artifacts were performed through the ACID toolbox for SPM12 [20, 21]. The preprocessing of DSC images consisted of motion correction and realignment of the time-series using the middle image as reference.

The IVIM fitting was performed in local python scripts (<https://github.com/inbrainlab/IVIMKurtosis>) using bi-exponential model [22] corrected for high b-values including the kurtosis contribution (K), which is described in Eq. 1. The kurtosis maps were obtained using the DTIFIT tool of FSL [23].

$$y(b_i) = \left\{ \left[f e^{-bD^*} + (1-f) e^{-bD + (bD)^2 \frac{K}{6}} \right]^2 + NCF \right\}^{1/2} \quad (1)$$

where $y(b_i)$ is the measured signal, D is the diffusion coefficient, D^* represents the pseudo-diffusion coefficient and f is the perfusion fraction. NCF represents the noise correction factor. After performing the fitting, fD^* maps were obtained by multiplying f and D^* maps. The robustness of the fitting was estimated by calculating the RMSE.

The DSC outputs as cerebral blood flow (CBF), cerebral blood volume (CBV), and mean transit time (MTT) maps were obtained with the Dynamic Susceptibility Contrast MRI toolbox for Matlab (<https://github.com/marcocastellaro/dsc-mri-toolbox>) by performing the semi-automatic arterial input function (AIF) selection [24] and the deconvolution of DSC curve [25].

Data analysis

Patients' images were independently reviewed and assessed by two neuroradiologists (M.C.Z.Z and A.C.S) for diagnosis purposes. The neuroradiologists also selected the appropriate slices to assess IVIM-derived maps and the corresponding slices for other imaging modalities. The specialists' reports were further confirmed with the results of the biopsies.

Quantitative measurements were performed in R [26] by extracting the voxelwise values of normalized DSC-CBF, diffusion coefficient, normalized fD^* and perfusion fraction maps within the ROIs of tumor border, tumor interior and edema (when present). The ROIs were manually drawn using the FSLeyes tool of FSL [23] considering multiple images modalities, as post-contrast T1w, post-contrast FLAIR and IVIM perfusion fraction to delineate regions of tumors' border, interior/necrosis and adjacent regions of edema. Contralateral ROIs were also selected in normal-appearing, contralateral regions. An illustrative example of the ROIs is shown in Supplementary Figure 9. Voxelwise correlations between normalized DSC-CBF and normalized fD^* and perfusion fraction for the same ROIs were performed.

Results

Figure 1 shows the fitting result of IVIM signal decay of a tumoral region for an illustrative patient, including the value of RMSE measurement. Table 2 shows the reports from two neuroradiologists based on all the acquired sequences except the IVIM images, analyzed separately. The histological reports and tumor grades are provided.

Next, we describe in detail relevant examples of microvascular and BBB tumoral alterations detected through IVIM (Figs. 2, 4 and 5). Images of the other patients are shown in the supplementary material. The quantitative measurements of IVIM outputs and normalized DSC-CBF are shown in Table 3 for all patients.

Figure 2 shows the images for patient 4 (Table 2) with a high-grade glioma. In this case, there is evidence of BBB disruption in the tumor borders (pointed by the red arrows), which is enhanced in the T1 post-contrast images (Fig. 2a). The same region also shows ITSS in SWI, indicating increased vascularization, also captured in DSC perfusion. In addition, IVIM f and fD^* maps displayed increased values

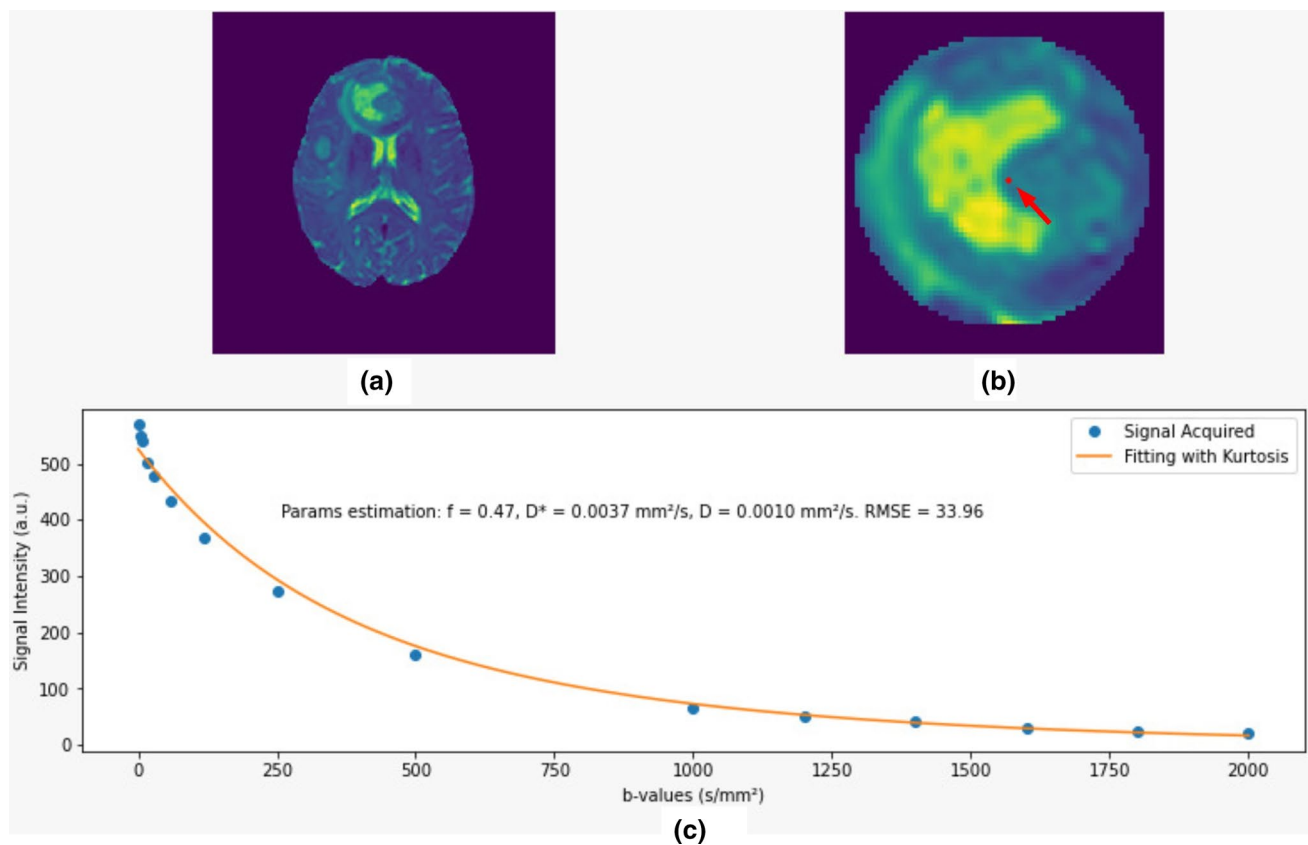


Fig. 1 **a** Raw IVIM data with $b=0$. **b** Zoomed tumor ROI. **c** The results of a bi-exponential fitting model for IVIM data signal decay corrected with the kurtosis contribution including the measure of RMSE for an illustrative voxel within the region shown in **(b)**

for these regions, suggesting sensitivity to BBB breakdown and neovascularity. Interestingly, in regions pointed by the yellow arrows, there is no clear evidence of BBB disruption according to T1 post-contrast images, but there are linear foci of increased f and fD^* values, suggesting increased local perfusion and BBB damage, also captured in the post-contrast FLAIR. Of importance, it was also possible to capture increased IVIM perfusion fraction in the extensive areas of abnormal FLAIR signal around and posterior to the tumor (pink arrow), which was not detectable through DSC-CBF or SWI. The same areas also did not show any pathological enhancement on post-contrast T1. The analysis of the quantitative measurements for patient 4 in the boxplots of Fig. 3 shows that increase in perfusion-related parameters are more evident for IVIM outputs in comparison to DSC-CBF. The diffusion coefficient maps in Fig. 2d show increased diffusion in regions with increased perfusion and decreased diffusion in regions of high cellularity, according to the expected in the literature of diffusion imaging for tumors [27].

The glioblastoma case in Fig. 4 clearly displays BBB breakdown, evident in areas of post-contrast enhancement on T1W images (Fig. 4a, yellow arrows). The red arrow in Fig. 4 indicates an area of low signal on SWI, high signal on FLAIR,

and absence of enhancement on post-contrast T1, interpreted as an area of necrosis, probably with a hemorrhagic component. While regions with viable tumoral tissue presented subtle increased perfusion on IVIM maps, the necrotic area did not (Fig. 4f and g). In areas of increased signal intensity on FLAIR located adjacent and posterior to the core of the tumor (pink arrow), we could detect increased perfusion fraction on IVIM maps. For regions where there is no BBB disruption, DSC-CBF could not capture increased blood flow.

For the LGG patient shown in Fig. 5, no evident disruption of BBB was detectable on post-contrast T1-weighted images. The subtle medial foci of apparent enhancement on the post-contrast T1 (yellow arrow), also visible on DSC CBF map, represents a vessel within the tumor, confirmed on reformatted images. The regions of ITSS in the SWI map (red arrows) are compatible with the increase IVIM perfusion signal intensity, suggesting neovascularization. Moreover, increased IVIM perfusion was also detected in the posterior areas of the tumor, which showed only increased signal on FLAIR (pink arrow), without corresponding ITSS or increased CBF. The quantitative measurements in the boxplots of Fig. 6 depict the sensibility of IVIM f and fD^* maps in detecting early changes in tumor's hemodynamic. Both the tumor's periphery

Table 2 Patients' information and specialists' reports based on MR imaging and histopathology

ID	Gender	Age	MRI report	Histological report	Grade
P01	Male	69	Right frontal and nucleocapsular expansive formation, compatible with high-grade primary neoplasm	Glioma grade 3 or 4	HGG
P02	Female	67	Findings compatible with neoplasm; central area suggestive of necrosis, multicentric, with increased perfusion and very high choline peaks. Glioblastoma	Glioma grade 3 or 4	HGG
P03	Female	71	Multiple lesions suggestive of neoplasia, with high cellularity and necrosis, with distribution in the edge of the ventricles, suggesting primary lymphoma of the CNS	Glioma grade 4 – GBM – IDH-wildtype	HGG
P04	Male	76	Expansive brain lesion suggestive of high-grade neoplasm	Glioma grade 3 or 4	HGG
P05	Male	59	Expansive lesion in the corpus callosum, compatible with high-grade glioma	Glioma grade 4 – GBM	HGG
P06	Female	38	Frontal expansive formation on the right compatible with high-grade glioma	Glioma grade 4 – GBM – IDH-wildtype	HGG
P07	Male	71	Expansive brain lesion suggestive of high-grade neoplasm	Glioma grade 4 – GBM	HGG
P08	Male	77	Left temporal expansive lesion with signs of aggressiveness, compatible with neoplasia and suggestive of high-grade glioma	Glioma grade 3 or 4	HGG
P09	Male	28	Left frontal intra-axial expansive lesion suggestive of low-grade glioma	Astrocytoma grade 2 – IDH-mutant (R132H)	LGG
P10	Male	33	Expansive left parietal lesion, compatible with the clinical hypothesis of low-grade glioma	Astrocytoma grade 2 – IDH-mutant	LGG
P11	Male	39	Temporoparietal expansive cortico-subcortical lesion on the left compatible with diffuse glioma	Oligodendroglioma grade 2	LGG
P12	Male	56	Expansive lesion, compatible with the clinical hypothesis of low-grade glioma	Glioma grade 2	LGG

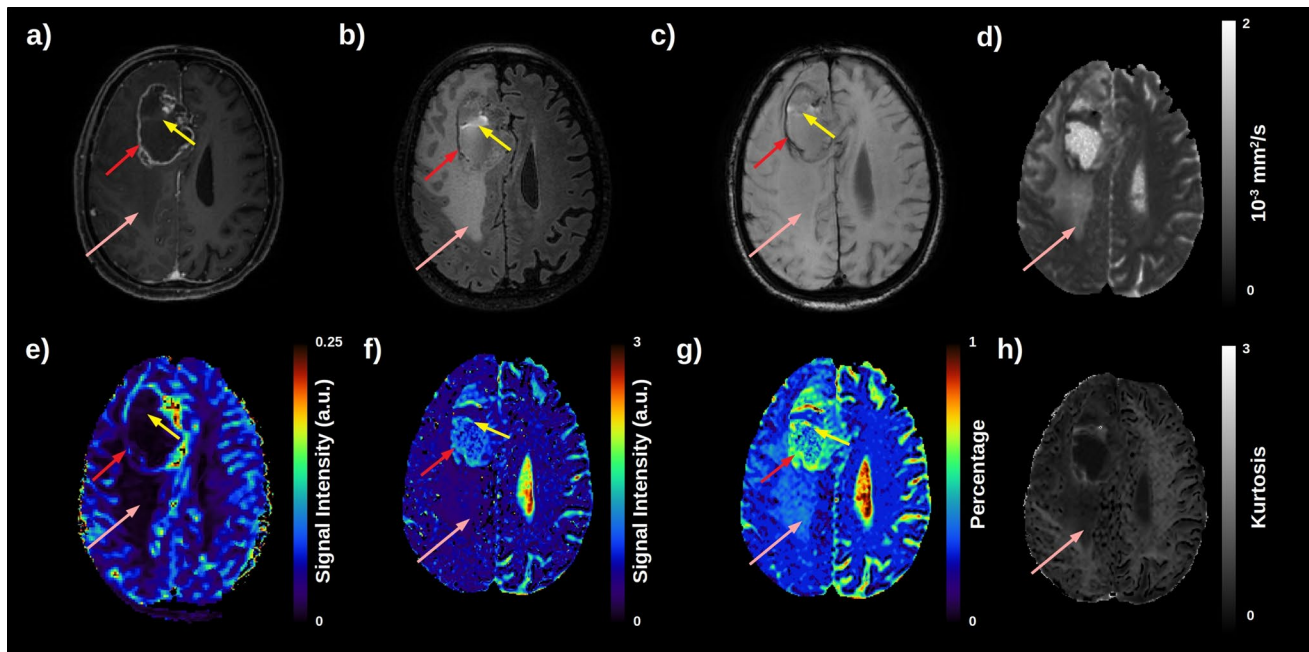


Fig. 2 High-grade glioma patient. **a** post-contrast T1-weighted image; **b** post-contrast FLAIR image; **c** susceptibility-weighted image; **d** Diffusion coefficient map **e** DSC CBF map; **f** IVIM fD^* map; **g** IVIM perfusion fraction map and **h** Map of diffusion kurtosis. The red arrow shows the tumor border in which there is BBB disruption. For the region pointed by the yellow arrow, there is no clear evidence

of increased perfusion or BBB damage in DSC or post-contrast T1 images, but findings from the SWI, post-contrast FLAIR, and IVIM suggested high neovascularity and possible BBB damage. The pink arrow displays increased IVIM perfusion in the more infiltrative, edema-like, posterior regions

Table 3 Quantitative measurements for normalized DSC-CBF (a.u.) and the IVIM outputs, diffusion coefficient (D) in mm^2/s , perfusion fraction (f) and fD^* (a.u.) maps for the ROIs of tumor border, tumor interior and the respective contra-lateral regions

	HGG1	HGG2	HGG3	HGG4	HGG5	HGG6	HGG7	HGG8	LGG1	LGG2	LGG3	LGG4
<i>Tumor border</i>												
CBF	0.66±0.14	0.45±0.19	0.5±0.17	0.24±0.15	0.6±0.18	0.64±0.2	0.32±0.28	0.41±0.2	0.59±0.14	0.19±0.17	0.59±0.15	0.65±0.14
D	0.73±0.06	0.93±0.09	1.19±0.29	2.24±0.27	0.72±0.09	0.77±0.23	0.94±0.39	1.11±0.37	1.39±0.24	1.44±0.18	0.85±0.09	1.11±0.31
f	0.17±0.05	0.35±0.09	0.52±0.13	0.35±0.09	0.24±0.06	0.17±0.07	0.22±0.06	0.41±0.16	0.19±0.08	0.3±0.06	0.19±0.09	0.3±0.05
fD^*	0.047±0.137	0.049±0.09	0.521±0.2	0.022±0.092	0.038±0.11	0.074±0.165	0.049±0.155	0.595±0.267	0.584±0.184	0.017±0.098	0.144±0.202	0.46±0.19
<i>Contra-lateral region of tumor border</i>												
CBF	0.65±0.23	0.68±0.16	0.38±0.14	0.24±0.12	0.68±0.16	0.39±0.22	0.33±0.23	0.37±0.24	0.49±0.26	0.43±0.18	0.55±0.15	0.5±0.2
D	0.64±0.05	0.66±0.06	0.55±0.19	0.76±0.1	0.77±0.16	0.56±0.14	0.69±0.12	0.59±0.1	0.57±0.14	0.69±0.18	0.71±0.08	0.61±0.13
F	0.2±0.09	0.2±0.04	0.2±0.09	0.24±0.06	0.27±0.1	0.23±0.15	0.29±0.11	0.19±0.07	0.26±0.13	0.3±0.2	0.21±0.13	0.21±0.1
fD^*	0.052±0.110	0.071±0.134	0.023±0.104	0.014±0.073	0.036±0.139	0.025±0.106	0.031±0.103	0.016±0.111	0.012±0.085	0.053±0.157	0.047±0.138	0.03±0.09
<i>Tumor interior</i>												
CBF	0.61±0.2	0.09±0.05	0.38±0.19	0.14±0.08	0.79±0.12	0.42±0.23	0.09±0.09	0.31±0.27	0.43±0.14	0.39±0.18	0.53±0.17	0.5±0.14
D	0.92±0.13	0.76±0.09	0.61±0.11	1.13±0.17	0.89±0.14	1.58±0.51	0.72±0.17	1.16±0.17	1.37±0.14	1.54±0.18	1.19±0.14	1.07±0.16
f	0.19±0.09	0.46±0.11	0.06±0.14	0.27±0.09	0.36±0.08	0.36±0.07	0.4±0.05	0.33±0.07	0.18±0.05	0.25±0.08	0.33±0.04	0.3±0.04
fD^*	0.073±0.169	0.532±0.272	0.029±0.157	0.521±0.082	0.092±0.101	0.598±0.194	0.649±0.151	0.345±0.118	0.115±0.052	0.093±0.242	0.582±0.148	0.01±0.05
<i>Contra-lateral region of tumor interior</i>												
CBF	0.76±0.14	0.36±0.23	0.56±0.14	0.25±0.16	0.59±0.1	0.62±0.16	0.18±0.19	0.43±0.13	0.27±0.22	0.51±0.17	0.59±0.16	0.49±0.2
D	0.8±0.14	0.8±0.1	1.75±0.33	0.63±0.26	1.22±0.07	0.51±0.04	0.98±0.16	0.88±0.2	0.56±0.09	0.68±0.08	0.65±0.17	0.71±0.21
f	0.2±0.06	0.05±0.18	0.63±0.09	0.24±0.12	0.23±0.03	0.2±0.02	0.21±0.09	0.4±0.19	0.23±0.1	0.04±0.07	0.2±0.15	0.21±0.13
fD^*	0.153±0.201	0.081±0.199	0.025±0.092	0.015±0.082	0.566±0.144	0.015±0.09	0.029±0.097	0.04±0.079	0.049±0.161	0.187±0.132	0.022±0.079	0.03±0.1

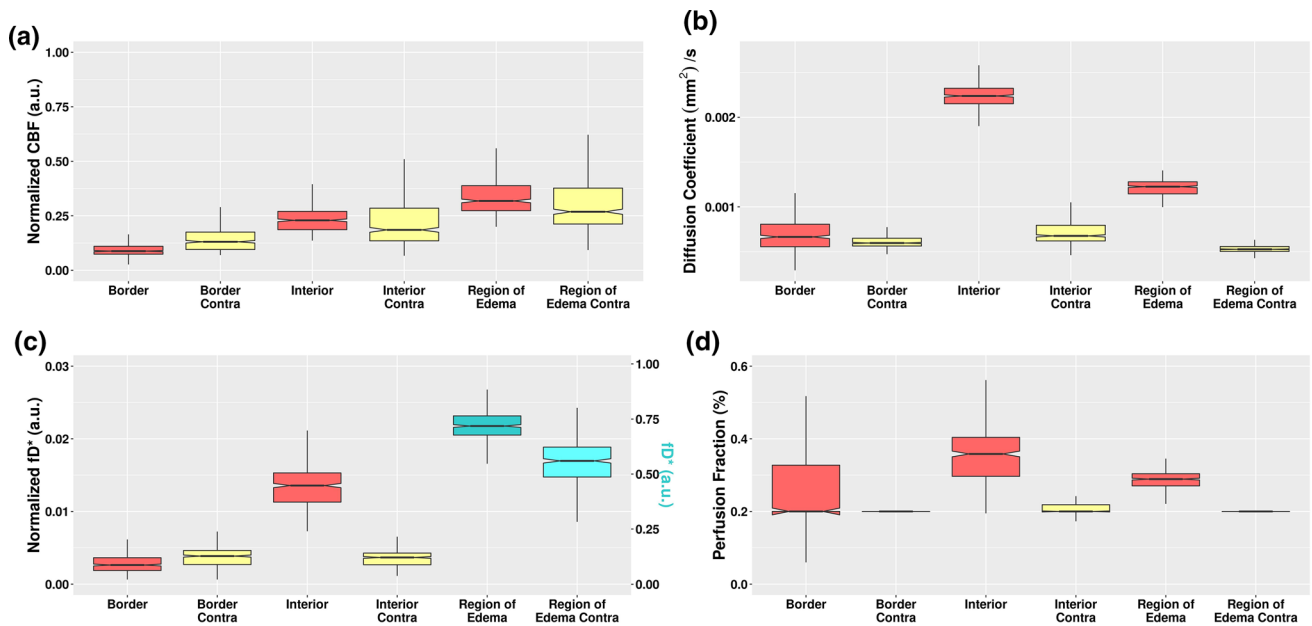
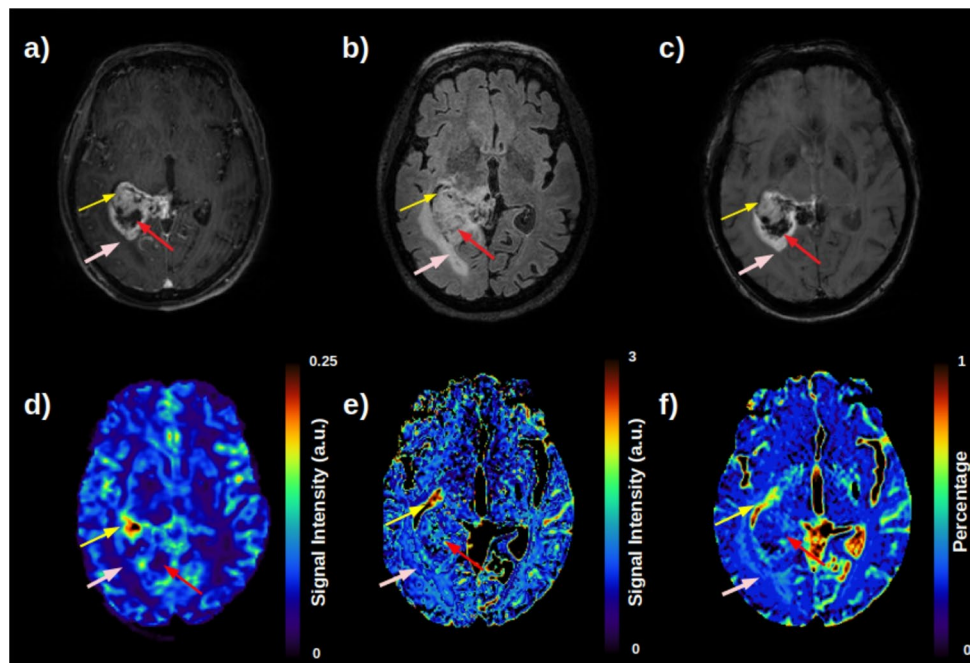


Fig. 3 Boxplots of quantitative measurements for **a** Normalized DSC-CBF, and the IVIM output maps of **b** Diffusion coefficient, **c** fD^* maps and **d** Perfusion fraction f for the ROIs of tumor border, tumor

interior and edema of the HGG patient of Fig. 2. For fD^* maps, the scale for regions of edema were higher than for Tumor border and interior, and therefore it was plotted in a secondary y axis in blue

Fig. 4 Glioblastoma patient. **a** post-contrast T1-weighted image; **b** post-contrast FLAIR image; **c** susceptibility-weighted image; **d** DSC CBF map; **e** IVIM fD^* map; **f** IVIM perfusion fraction map. The yellow arrow shows areas of BBB disruption within the tumor. The red arrow points to areas of necrosis. The pink arrow shows region of increased perfusion fraction within areas of edema-like



and central regions show a great increase in f and fD^* values, compared to normal-appearing contra-lateral regions.

The correlation analysis between DSC-CBF and IVIM perfusion-related maps in Table 4 showed no significant correlation for almost all the patients. For most of them, the correlation coefficients were close to zero or slightly negative.

Discussion

In general, for high-grade glioma patients, IVIM maps were able to detect regions with BBB breakdown, in agreement with post-contrast T1W images, and demonstrated increased perfusion in regions that also showed increased

Fig. 5 Low-grade glioma patient. **a** post-contrast T1-weighted image; **b** post-contrast FLAIR image; **c** susceptibility-weighted image; **d** DSC CBF map; **e** IVIM fD^* map; **f** IVIM perfusion fraction map. No evidence of BBB damage in post-contrast T1-weighted images. IVIM maps showed increase perfusion in regions of high ITSS in the susceptibility-weighted image, compared to the normal contralateral hemisphere

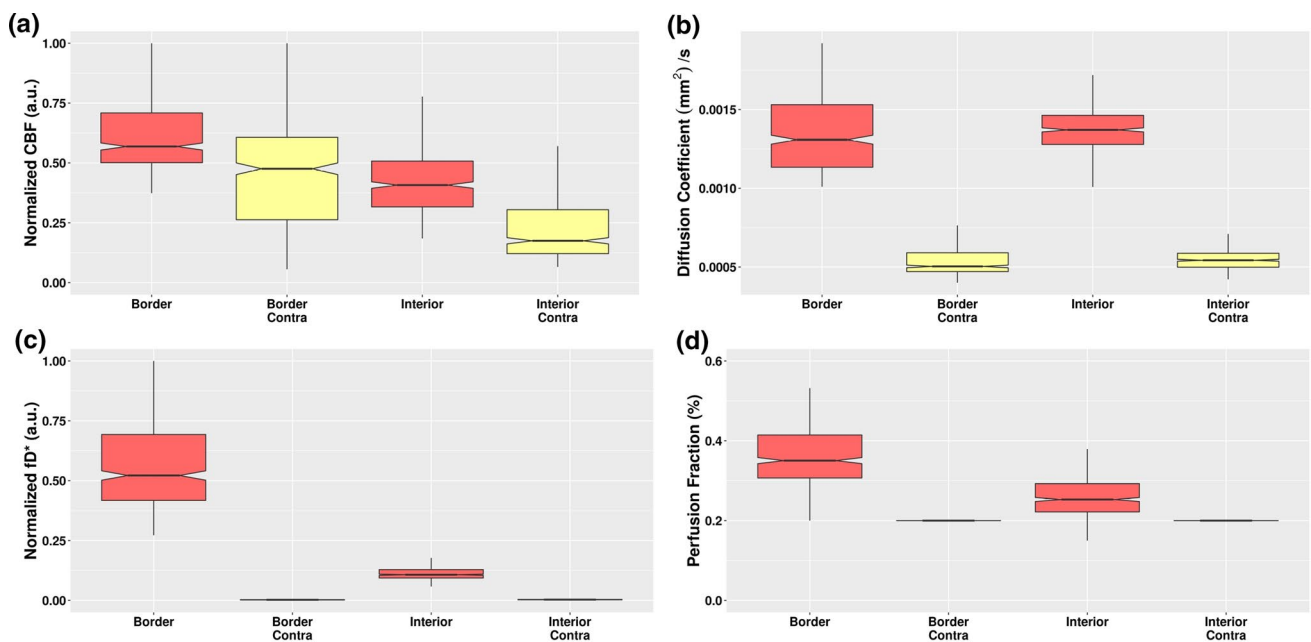
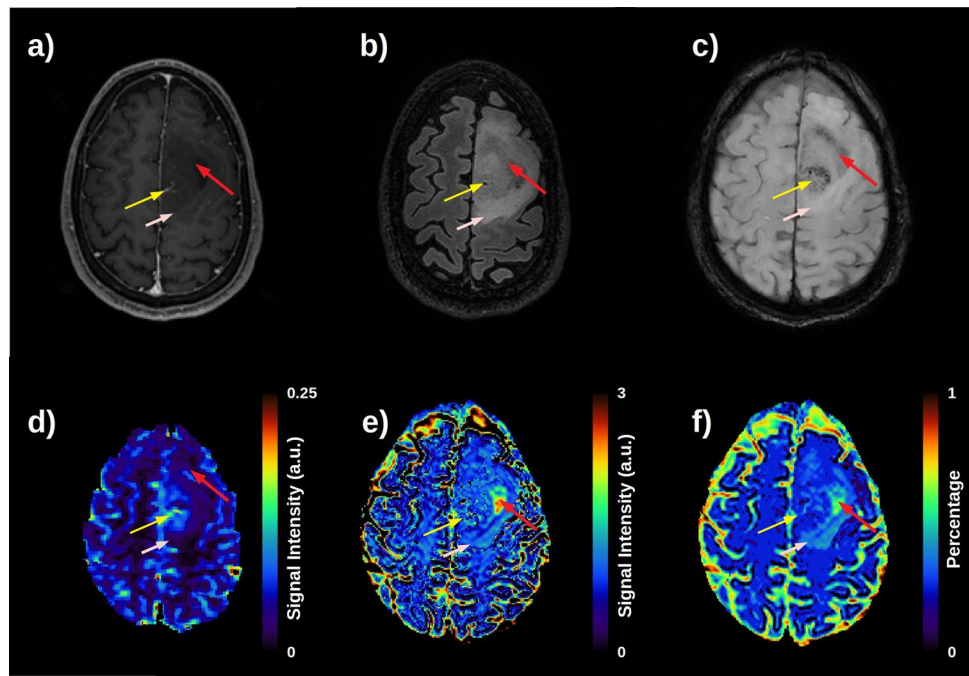


Fig. 6 Boxplots of quantitative measurements for **a** Normalized DSC-CBF, and the IVIM output maps of **b** Diffusion coefficient, **c** fD^* and **d** Perfusion fraction f for the ROIs of tumor border and tumor interior of the LGG patient of Fig. 5

ITSS on SWI, therefore interpreted as neovascularity. Moreover, IVIM perfusion fraction and fD^* maps showed hyperintensity within edema-like areas, not apparent in DSC CBF maps. In LGG patients, IVIM perfusion-related maps were sensitive to detect perfusion changes due to neovascularity, in agreement with ITSS changes on SWI.

BBB breakdown and increased vascular demand with intratumoral neovascularization are common features in HGG, detectable through different MRI techniques. This study focused on investigating how these changes manifest in IVIM f and fD^* maps. We further investigated whether this novel technique could detect hemodynamic changes typical of HGG within LGG, indicating a potential role in

Table 4 Results for the correlation between normalized DSC-CBF and IVIM f and fD^* maps in their ROIs of tumor interior and tumor border

	Tumor border		Tumor interior	
	CBF x f	CBF x fD^*	CBF x f	CBF x fD^*
HGG1	0.30	-0.28	-0.65	0.40
HGG2	0.12	0.01	-0.76	-0.68
HGG3	0.10	0.05	0.27	-0.04
HGG4	0.20	0.06	0.23	0.01
HGG5	0.18	0.19	0.61	0.05
HGG6	0.22	-0.13	0.01	0.30
HGG7	-0.17	0.21	0.09	0.10
HGG8	-0.61	-0.64	-0.32	-0.23
LGG1	-0.39	-0.47	-0.08	0.06
LGG2	-0.02	0.10	-0.02	-0.16
LGG3	-0.38	-0.03	0.01	0.19
LGG4	-0.13	0.41	-0.03	0.31

predicting more aggressive behavior and possibly worse prognosis. Several key findings emerge from the present study. First, IVIM maps are sensitive to increased microvascular density in regions with corresponding ITSS. Second, IVIM maps detected increased perfusion in areas of BBB disruption, characterized as foci of contrast enhancement in T1-weighted images. Third, IVIM was sensitive to areas of abnormal perfusion within LGG. Finally, IVIM was the only MRI modality showing abnormalities in peritumoral areas, where only increased FLAIR signal was evident.

Starting with HGG patients' analysis, the first finding is the increased IVIM perfusion in the tumor border (Fig. 2, red arrow). In this region, an enhanced signal in post-contrast T1-weighted images represents a viable hyperproliferative tumor whose increased demand for blood supply led to neovascularization and BBB breakdown. BBB disruption becomes evident by the extravasation of gadolinium from the intravascular compartment into tumoral tissues, perceived as areas of contrast enhancement [28]. In such regions, DSC-CBF was sensitive to increased perfusion, as well as IVIM maps, which agrees with previous studies [12, 14]. In that sense, increased perfusion fraction f maps reflected the increased blood content within the tumor even in regions with intact BBB function. Increased values in fD^* maps suggest increased regional neovascularization, which is confirmed by analyses of susceptibility-weighted images that exhibit ITSS in the same regions of increased signal in IVIM perfusion-related maps. In the boxplots of Fig. 3, the perfusion fraction f was the most sensitive perfusion measurement to detect increase in blood flow in the tumor border, and both f and fD^* maps showed higher vascularization in the tumor's core.

Another interesting contribution of IVIM maps in HGG cases is the analysis of adjacent regions with abnormal T2

signals in FLAIR. For example, in patient 4, shown in Fig. 2, areas of hyperintensity in FLAIR extend over a large portion of the right hemisphere. Moreover, in the T2 hyperintense areas surrounding the necrotic lesion in Fig. 2b, there was also no evidence of BBB breakdown in post-contrast T1, nor of increased CBF in DSC maps or ITSS in SWI. However, IVIM f and fD^* maps showed increased signal in those areas. In such cases, f and fD^* maps could either be capturing subtle perfusional changes of underlying viable tissue or could be capturing remnants of edema, secondary to IVIM imperfect fitting. When planning surgical approaches in these cases, an important question lies in distinguishing areas that harbor viable neoplastic tissue that should be removed, responsible for future progression/recurrence, from areas representing just vasogenic edema. In this context, histopathological studies are necessary to investigate what tissue abnormalities underlie the increased perfusional fraction detected through IVIM on edema-like peritumoral regions. If viable tumoral tissue is detected in those regions, then IVIM probably offers an added value in delineating tumoral extent, outperforming other MRI techniques in detecting vascular changes that precede BBB leakage. In addition, among other HGG cases (supplementary material), foci of increased IVIM perfusion were found in regions of necrosis, which could also potentially represent remnant microvasculature and viable tumoral tissue [29].

Since IVIM was able to detect BBB damage and increased neovascularization in HGGs from our sample, we sought to analyze its performance in LGGs. The example in Fig. 5 refers to an IDH-mutant LGG case, in which post-contrast T1W images show no BBB breakdown, and the DSC-CBF map did show a subtle increase in perfusion within the tumor. IVIM f and fD^* maps showed increased signal in the tumor's borders, in agreement to regions of ITSS on SWI and inside the tumor, reflecting hemodynamic changes considered atypical for slow-growing tumors and more in line with HGG. This finding exemplifies how IVIM might be useful in identifying more aggressive LGGs, with potential for early progression and a worse prognosis.

The analysis of the correlation between DSC-CBF and IVIM perfusion maps showed no significant correlation for most of the patients for both tumor interior and tumor borders. This lack of correlation points toward the conclusion that the perfusion measurements of DSC and IVIM are not the same, reinforcing complementary microvascular information provided by the IVIM acquisition.

Our study has several limitations, mostly related to our small sample size, which precluded statistical analyses. Regarding the IVIM protocol, b0 images with the blips of phase-encoding in both anterior–posterior and posterior–anterior directions were not acquired, and hence the top up correction for susceptibility artifacts could not be performed [30, 31]. Moreover, slice thickness of 5 mm may result in partial

voluming, and can be pointed out as another methodological limitation. Importantly, we interpreted the regional IVIM perfusional changes observed within the gliomas based on how they correlate with neuroimaging findings from other MRI techniques. However, the current understanding of IVIM's biological meaning is still limited. Studies using MRI-guided histopathology sampling would be particularly useful to assess which pathological changes underlie the perfusional alterations detected through IVIM. Longitudinal studies confirming progression of suspicious areas could also be useful in understanding the meaning of early IVIM perfusional changes. Therefore, our results should be regarded as preliminary and warrant confirmation in larger and longitudinal samples, ideally with MRI-guided histopathological correlation.

Nonetheless, our study examined a well-characterized and pathologically confirmed cohort, comparing IVIM's findings against other, more established, MRI techniques, allowing for comparisons and biological inferences.

In conclusion, our initial findings suggest that IVIM maps may offer clinically relevant information that could potentially help guide therapeutic decisions in patients with gliomas. By detecting microvascular perfusion changes in areas displaying nonspecific signal abnormalities, IVIM could help better delineate the extent of the underlying tumor tissue and monitor its progression in size and histological grade. Future studies are needed to confirm our observations and to further assess the potential role of IVIM maps as neuroimaging biomarkers in the field of neuro-oncology.

Supplementary Information The online version contains supplementary material available at <https://doi.org/10.1007/s10334-021-00987-0>.

Acknowledgements This work was supported by Sao Paulo Research Foundation (FAPESP) (process number: 2019/06148-6) and by the Conselho Nacional de Desenvolvimento Científico e Tecnológico (CNPq) (process number: 151245/2019-3).

Author contributions AMP, ACS and RFL contributed to the study conception and design. Material preparation, data collection was performed by AMP. Data processing was performed by AMP and LMC. Data analysis was performed by AMP, MCZZ, ACS and RFL. The first draft of the manuscript was written by AMP, critical revision was performed by MCZZ and all authors commented on previous versions of the manuscript. All authors read and approved the final manuscript.

Declarations

Conflict of interest The authors declare no competing interests.

Ethical statement Twelve patients (8 HGG, 4 LGG; mean age \pm standard deviation (SD) = 56.11 ± 19.14) participated in this cross-sectional study, approved by the Institutional Review Board, after signing the informed consent agreement

References

- Louis DN, Perry A, Reifenberger G, von Deimling A, Figarella-Branger D, Cavenee WK, Ohgaki H, Wiestler OD, Kleihues P, Ellison DW (2016) The 2016 World Health Organization classification of tumors of the central nervous system: a summary. *Acta Neuropathol* 131:803–820
- Wang X, Cao M, Chen H, Ge J, Suo S, Zhou Y (2020) Simplified perfusion fraction from diffusion-weighted imaging in preoperative prediction of IDH1 mutation in WHO grade II-III gliomas: Comparison with dynamic contrast-enhanced and intravoxel incoherent motion MRI. *Radiol Oncol* 54:301–310
- Wang C, Dong H (2020) Ki-67 labeling index and the grading of cerebral gliomas by using intravoxel incoherent motion diffusion-weighted imaging and three-dimensional arterial spin labeling magnetic resonance imaging. *Acta radiol* 61:1057–1063
- Paschoal AM, Leoni RF, dos Santos AC, Paiva FF (2018) Intravoxel incoherent motion MRI in neurological and cerebrovascular diseases. *NeuroImage Clin*. <https://doi.org/10.1016/j.nicl.2018.08.030>
- Hsu CCT, Watkins TW, Kwan GNC, Haacke EM (2016) Susceptibility-weighted imaging of glioma: update on current imaging status and future directions. *J Neuroimaging* 26:383–390
- Su CQ, Lu SS, Han QY, Zhou MD, Hong XN (2019) Integrating conventional MRI, texture analysis of dynamic contrast-enhanced MRI, and susceptibility weighted imaging for glioma grading. *Acta radiol* 60:777–787
- Le Bihan D, Breton E, Lallemand D, Grenier P, Cabanis E, Laval-Jeantet M (1986) MR imaging of intravoxel incoherent motions: application to diffusion and perfusion in neurologic disorders. *Radiology* 161:401–407
- Detre JA, Leigh JS, Williams DS, Koretsky AP (1992) Perfusion imaging. *Magn Reson Med* 23:37–45
- Alsop DC, Detre JA, Golay X, Gunther M, Hendrikse J, Hernandez-Garcia L, Lu H, MacIntosh BJ, Parkes LM, Smits M, van Osch MJ, Wang DJ, Wong EC, Zaharchuk G (2015) Recommended implementation of arterial spin-labeled perfusion MRI for clinical applications: A consensus of the ISMRM perfusion study group and the European consortium for ASL in dementia. *Magn Reson Med* 73:102–116
- Detre JA, Rao H, Wang DJ, Chen YF, Wang Z (2012) Applications of arterial spin labeled MRI in the brain. *J Magn Reson Imaging* 35:1026–1037
- Wolf RL, Wang J, Wang S, Melhem ER, O'Rourke DM, Judy KD, Detre JA (2005) Grading of CNS neoplasms using continuous arterial spin labeled perfusion MR imaging at 3 Tesla. *J Magn Reson Imaging* 22:475–482
- Bisdas S, Koh TS, Roder C, Braun C, Schittenhelm J, Ernemann U, Klose U (2013) Intravoxel incoherent motion diffusion-weighted MR imaging of gliomas: feasibility of the method and initial results. *Neuroradiology* 55:1189–1196
- Federau C, O'Brien K, Meuli R, Hagmann P, Maeder P (2014) Measuring brain perfusion with intravoxel incoherent motion (IVIM): initial clinical experience. *J Magn Reson Imaging* 39:624–632
- Federau C, Meuli R, O'Brien K, Maeder P, Hagmann P (2014) Perfusion Measurement in Brain Gliomas with Intravoxel Incoherent Motion MRI. *Am J Neuroradiol* 35:256–262
- Shen N, Zhao L, Jiang J, Jiang R, Su C, Zhang S, Tang X, Zhu W (2016) Intravoxel incoherent motion diffusion-weighted imaging analysis of diffusion and microperfusion in grading gliomas and comparison with arterial spin labeling for evaluation of tumor perfusion. *J Magn Reson Imaging* 44:620–632
- Li WF, Niu C, Shakir TM, Chen T, Zhang M, Wang Z (2018) An evidence-based approach to assess the accuracy of intravoxel

- incoherent motion imaging for the grading of brain tumors. Med (United States). <https://doi.org/10.1097/MD.00000000000013217>
17. Yan LF, Sun YZ, Zhao SS, Hu YC, Han Y, Li G, Zhang X, Tian Q, Liu ZC, Yang Y, Nan HY, Yu Y, Sun Q, Zhang J, Chen P, Hu B, Li F, Han TH, Wang W, Bin CG (2019) Perfusion, diffusion, or brain tumor barrier integrity: Which represents the glioma features best? *Cancer Manag Res* 11:9989–10000
 18. Gu T, Yang T, Huang J, Yu J, Ying H, Xiao X (2021) Evaluation of gliomas peritumoral diffusion and prediction of IDH1 mutation by IVIM-DWI. *Aging (Albany NY)* 13:9948–9959
 19. Dubois LG, Campanati L, Righy C, D'Andrea-Meira I, e Spohr TCL de S, Porto-Carreiro I, Pereira CM, Balça-Silva J, Kahn SA, DosSantos MF, Oliveira M de AR, Ximenes-da-Silva A, Lopes MC, Faveret E, Gasparetto EL, Moura-Neto V (2014) Gliomas and the vascular fragility of the blood brain barrier. *Front Cell Neurosci* 8:1–13
 20. Mohammadi S, Möller HE, Kugel H, Müller DK, Deppe M (2010) Correcting eddy current and motion effects by affine whole-brain registrations: Evaluation of three-dimensional distortions and comparison with slice-wise correction. *Magn Reson Med*. <https://doi.org/10.1002/mrm.22501>
 21. Ruthotto L, Kugel H, Olesch J, Fischer B, Modersitzki J, Burger M, Wolters CH (2012) Diffeomorphic susceptibility artifact correction of diffusion-weighted magnetic resonance images. *Phys Med Biol* 57:5715–5731
 22. Le Bihan D (2019) What can we see with IVIM MRI? *Neuroimage*. <https://doi.org/10.1016/j.neuroimage.2017.12.062>
 23. Jenkinson M, Beckmann CF, Behrens TEJ, Woolrich MW, Smith SM (2012) FSL. *Neuroimage* 62:782–790
 24. Peruzzo D, Bertoldo A, Zanderigo F, Cobelli C (2011) Automatic selection of arterial input function on dynamic contrast-enhanced MR images. *Comput Methods Programs Biomed* 104:e148–e157
 25. Zanderigo F, Bertoldo A, Pillonetto G, Cobelli C (2009) Nonlinear stochastic regularization to characterize tissue residue function in bolus-tracking MRI: Assessment and comparison with SVD, block-circulant SVD, and tikhonov. *IEEE Trans Biomed Eng* 56:1287–1297
 26. Team R core (2021) R: A Language and Environment for Statistical Computing
 27. Kang Y, Choi SH, Kim YJ, Kim KG, Sohn C-H, Kim J-H, Yun TJ, Chang K-H (2011) Gliomas : Histogram analysis of apparent diffusion coefficient maps purpose : methods : results. *Radiology* 261:882–890
 28. Kiviniemi A, Gardberg M, Ek P, Frantzén J, Bobacka J, Minn H (2019) Gadolinium retention in gliomas and adjacent normal brain tissue: association with tumor contrast enhancement and linear/macrocyclic agents. *Neuroradiology* 61:535–544
 29. Brat DJ, Van Meir EG (2004) Vaso-occlusive and prothrombotic mechanisms associated with tumor hypoxia, necrosis, and accelerated growth in glioblastoma. *Lab Invest* 84:397–405
 30. Andersson JLR, Skare S, Ashburner J (2003) How to correct susceptibility distortions in spin-echo echo-planar images: Application to diffusion tensor imaging. *Neuroimage* 20:870–888
 31. Smith SM, Jenkinson M, Woolrich MW, Beckmann CF, Behrens TEJ, Johansen-Berg H, Bannister PR, De Luca M, Drobnjak I, Flitney DE, Niazy RK, Saunders J, Vickers J, Zhang Y, De Stefano N, Brady JM, Matthews PM (2004) Advances in functional and structural MR image analysis and implementation as FSL. *Neuroimage* 23:208–219

Publisher's Note Springer Nature remains neutral with regard to jurisdictional claims in published maps and institutional affiliations.